Detection of magnetic circular dichroism with subnanometer convergent electron beams

Thomas Thersleff,[1,*] Ján Rusz,[2,†] Björgvin Hjörvarsson,[2,‡] and Klaus Leifer[1,§]
[1]*Department of Engineering Sciences, Uppsala University, Box 534, 75121 Uppsala, Sweden*
[2]*Department of Physics and Astronomy, Uppsala University, Box 516, 75120 Uppsala, Sweden*
(Received 17 June 2016; revised manuscript received 13 August 2016; published 28 October 2016)

The electron energy-loss spectroscopy technique known as electron magnetic circular dichroism (EMCD) has enormous potential for quantitatively probing the magnetic behavior of materials on the nanoscale. However, the requirement for mostly parallel illumination conditions greatly complicates the extraction of EMCD signals from surface areas under a few square nanometers, because scanning probe methods are limited to around this spatial resolution by the need for higher convergence angles. Here we propose theoretically and demonstrate experimentally that EMCD detection is feasible with convergence angles that are sufficiently large even for atomic resolution spectroscopy. Utilizing scanning transmission electron microscopy we experimentally detect a clear EMCD signal from a 50-nm-thick sample of bcc iron using a convergence semiangle of 8 mrad at 300 keV acceleration voltage, resulting in a probe size of approximately 2 Å. We subsequently estimate the number of chirally scattered electrons needed for an unambiguous detection of the EMCD signal and present a method to quantify confidence in signal detection.

DOI: 10.1103/PhysRevB.94.134430

I. INTRODUCTION

One of the most important strategic goals in the field of nanomagetism research is the exploitation of nanoscale confinement effects, potentially enabling devices with properties unachievable in bulk magnets [1]. Innovation in this direction requires a comprehensive understanding of the fundamental underlying mechanisms giving rise to emergent magnetic effects. The detection and, hence, understanding of these phenomena require experimental techniques capable of resolving spin and orbital magnetic moments on the length scales from which they originate, namely, subnanometer.

These challenges can be met through the use of electron energy-loss spectroscopy (EELS) using a technique known as electron energy-loss magnetic circular dichroism (EMCD) [2]. EMCD can be considered the electron analogy to x-ray magnetic circular dichroism (XMCD) with the very important exception that it utilizes electrons as the probe particles rather than photons. The charged nature of electrons allows coherent electron beams to be strongly focused with the use of electromagnetic lenses, enabling acquisition of real-space images that transfer information down to the Ångström scale. Another key difference is that while XMCD utilizes circularly polarized synchrotron radiation to achieve dichroic absorption spectra in magnetic materials, EMCD instead utilizes the sample itself as a beam splitter to achieve a comparable dichroic effect [2]. However, as with XMCD, sum rules can be applied to EMCD spectra to quantify the magnetic orbital to spin moment ratio m_L/m_S [3,4]. Hence EMCD yields comparable data to XMCD, but with a much higher spatial resolution and implementation on any transmission electron microscope (TEM) equipped with an EELS spectrometer. Accordingly, EMCD holds the promise of becoming a powerful complementary technique to XMCD, probing length scales that are presently unachievable with x rays and dramatically bolstering our fundamental understanding of nanoscale magnetic behavior.

Traditionally, the design of EMCD experiments calls for parallel illumination. This is motivated by the two-beam geometry proposed in 2003 [5], where one aims for a coherent superposition of two interfering plane waves, propagating through the sample. The EMCD can then be detected as the difference of two EELS spectra acquired at specific scattering angles, lying on a so-called Thales circle, which is circumscribed to the two plane waves in the diffraction plane [2,5]. Were the incident electron wave strongly converged, the sharp spots in the diffraction plane would blur into disks. Particularly, as one approaches the convergence needed for atomic resolution, where the diffracted discs overlap, it has been naturally assumed that the EMCD signal at Thales circle positions spreads and weakens in relative terms [6,7], thereby presenting a fundamental limit to spatial resolution.

This requirement for parallel illumination has had a major impact on the design of EMCD experiments. Typically, the electron probe is converged to a diameter of some tens of nanometers and remains stationary for the duration of the entire experiment. This can result in quantitative information [8,9] but requires a high stability and runs the risk of beam damage, while not improving spatial resolution dramatically beyond what is presently possible with XMCD [10,11]. Energy-filtered diffraction patterns can be used to obtain quantitative information [12], but the lateral sampling diameter is limited to around 10 nm [13]. Energy-filtered TEM (EFTEM) images can be acquired to produce real-space maps of magnetic transitions [14,15]; however, these have not yet provided quantitative magnetic information.

An alternative experimental design that was first applied in 2008 [6] and experimentally expanded in recent studies [16–18] utilizes scanning TEM (STEM). STEM involves scanning a finely focused probe of electrons across a thin lamella and can be used to generate EEL spectrum images that contain chemical information from individual atomic columns.

*thomas.thersleff@mmk.su.se
†Jan.Rusz@physics.uu.se
‡Bjorgvin.Hjorvarsson@physics.uu.se
§Klaus.Leifer@angstrom.uu.se

For EMCD experiments, this experimental design conveys significant advantages. The use of a scanning probe reduces the dwell time on any given sample position to well below 1 s, while the low signal-to-noise ratio (SNR) in any given pixel can be compensated for by summing over an arbitrarily large number of individual spectra. This can increase the effective sample exposure time up to hours while mitigating the problem of beam damage. The spatial resolution of the STEM technique is determined by the diameter of the electron probe, and this is limited by the highest coherent convergence angle that can be achieved on the instrument. While recent developments with probe aberration correctors have enabled the generation of coherent probes with convergence angles upwards of 30 mrad or more [19,20], the requirement of near parallel illumination for EMCD experiments limits the convergence angle to approximately 3 mrad, corresponding to a spatial resolution of around 1 nm. This spatial resolution has been tested on a custom-fabricated Fe multilayer system; however, the range of electron-optical configurations compatible with EMCD has not been reported in detail. Hence, it is unknown to what extent the incident electron wave can be converged and, thus, what the ultimate fundamental spatial resolution of the EMCD technique is.

Here we explicitly explore the range of electron-optical configurations that are compatible with the generation and detection of an EMCD signal using the STEM-EMCD experimental design. Theoretical simulations reveal that EMCD can be detected with convergent electron beams having convergence angles well beyond 3 mrad. We find that an EMCD signal strength of up to 5% can be expected at 300-kV acceleration voltage for convergence angles up to 15 mrad in bcc iron, in principle allowing for the resolution of individual atomic planes. Experimental evidence confirms this by detecting EMCD using an electron-optical configuration sufficient to generate a probe with a FWHM of approximately 2 Å. Utilizing the large STEM-EEL spectrum images acquired in a three-beam orientation [6,12], we explore the minimum quantity of chirally scattered primary electrons needed to qualitatively detect an EMCD signal with this experimental configuration, subsequently relating this to the lateral scanning area for this experiment

II. SIMULATIONS

We have performed simulations of the inelastic electron scattering of convergent electron beams for a bcc iron sample. The combined multislice/Bloch-waves approach has been used [21], assuming an ideal aberration-corrected convergent electron beam with convergence angles from 1 mrad up to 15 mrad at an acceleration voltage of 300 kV. A bcc iron supercell with c axis parallel to the [075] direction has been constructed. This corresponds to a tilt of about 10 deg from the [011] zone axis to a symmetric three-beam orientation of the crystal for the beam propagating along the z direction, parallel to the supercell c axis [see Fig. 1(a)]. The systematic row of reflections is parallel to reciprocal lattice vector $\mathbf{G} = (200)$.

The resulting orthogonal supercell contains 148 atoms and its cell parameters are $a \times \sqrt{74}a \times \sqrt{74}a$, where $a = 2.87$ Å is the lattice parameter of bcc iron. Supercell axes correspond to crystallographic directions [100], [0$\bar{5}$7], and

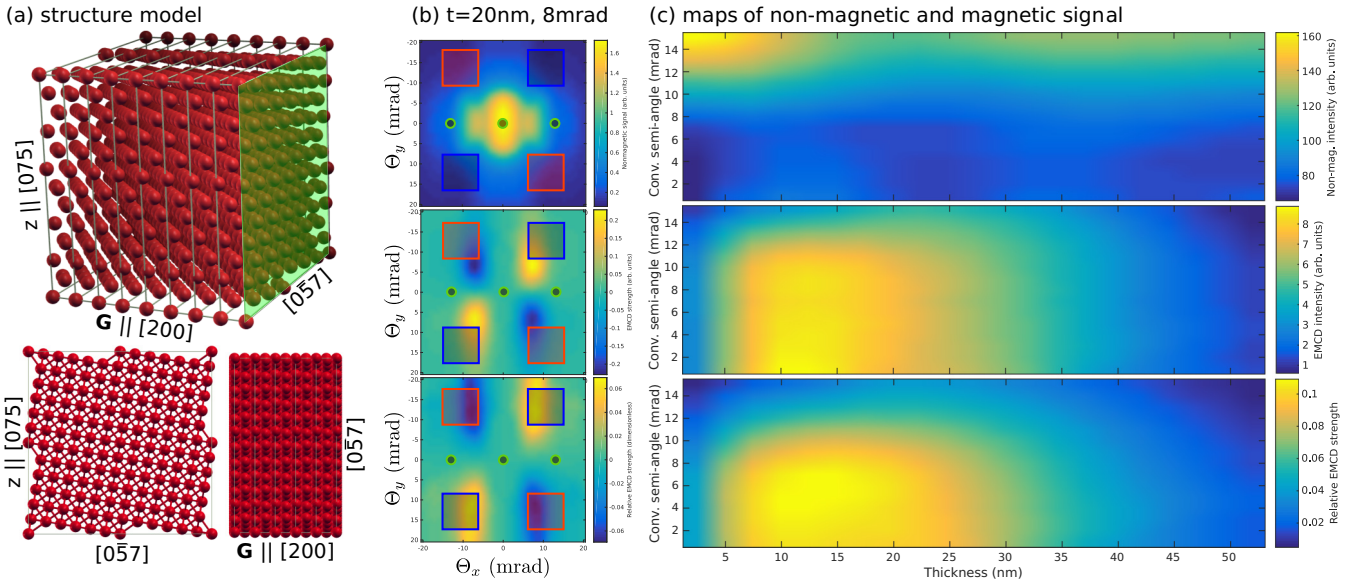

FIG. 1. (a) Structure model of bcc iron tilted into a three-beam orientation with $\mathbf{G} = (200)$, having the incoming electron beam tilted by about 10 deg from the (011) zone axis orientation. The beam is parallel to the z axis, which corresponds to the crystallographic direction [075]. A perspective view of the supercell (top) shows a (200) plane in green color. A side view (bottom left) is perpendicular to the (200) plane, and a top view (bottom right) shows (200) planes as vertical stripes of atoms. (b) Example of energy-filtered diffraction patterns of the iron L_3 edge, calculated at 300 kV acceleration voltage, 8 mrad convergence semiangle, and thickness $t = 20$ nm. Centers of transmitted beam and Bragg spots are marked by small green circles. Detector apertures are denoted by blue and red squares. Diffraction patterns span a range of ±20 mrad in both x, y directions, and from top to bottom is shown the nonmagnetic part of the signal, magnetic (EMCD) signal, and a relative EMCD signal strength, respectively. (c) Summary plots of nonmagnetic, magnetic, and relative magnetic signal for sample thicknesses up to 51.9 nm and convergence semiangles up to 15 mrad.

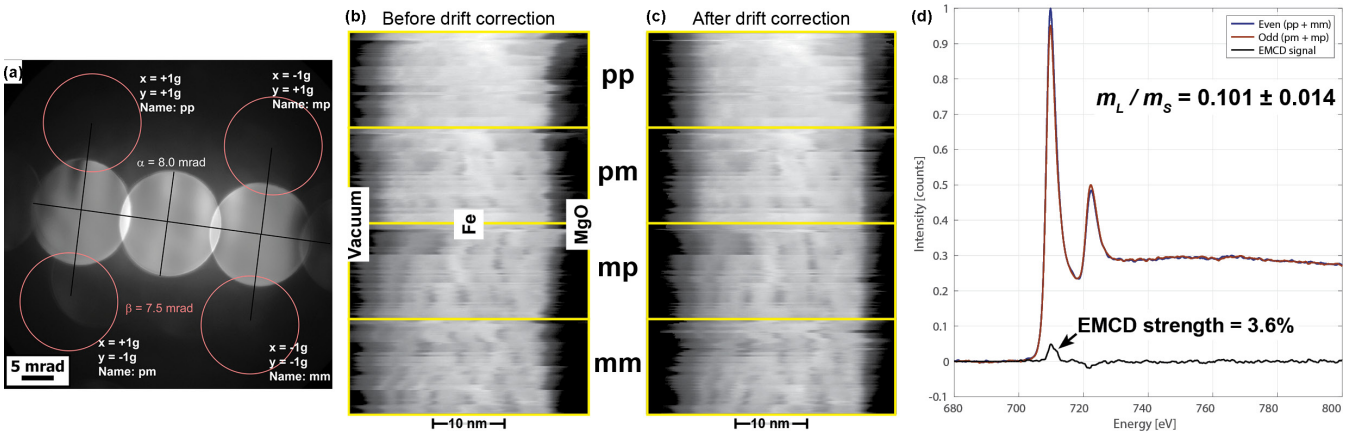

FIG. 2. (a) Experimentally obtained diffraction conditions for EMCD on Fe with a convergence angle of 8 mrad. The sample is oriented for the three-beam condition $\mathbf{g} = (002)$ and four datacubes were acquired. The spatial drift of the probe in all four datacubes before (b) and after (c) a custom-written drift-correction routine is applied. The EMCD signal from the double-difference method on this dataset (d) shows a signal strength of 3.6%.

[075], respectively. The electron beam is parallel to the c axis of the supercell, i.e., the [075] crystallographic direction of bcc iron. The length of the supercell c axis is 2.47 nm, and for thicker samples the supercell was repeated in the z direction. The range of treated sample thicknesses was from 2.47 to 51.9 nm. The lateral size of the entire simulation cell for multislice calculation was 5.17 nm $\times$ 4.94 nm, which is an 18 $\times$ 2 lateral periodic repetition of the structure model, sampled on a grid of 756 $\times$ 720. The inelastic scattering summation cutoff [21] was set to 10^{-6}. Resulting diffraction patterns were evaluated in the range of $\pm$20 mrad in both $\Theta_{x,y}$ scattering directions with a step of 1 mrad. See Fig. 1(b) for example energy-filtered diffraction patterns for the L_3 edge of bcc iron.

The main results of the simulations are summarized in Fig. 1(c). The three panels, from top to bottom, show the predicted nonmagnetic part of the Fe-L_3 signal, the magnetic (EMCD) part of the Fe-L_3 signal, and their ratio —the relative EMCD strength. The EMCD signal has been evaluated at fixed detector positions, as indicated in Fig. 1(b). These detector positions and sizes are in general not optimal. It would be certainly feasible to run a detailed simulation of the signal-to-noise ratio based on calculated images and find for each calculated combination of thickness and convergence angles the optimal conditions [22]. However, in a practical situation, when an experimentalist takes a new unknown sample, this information is not available. Therefore we have decided on a simple and pragmatic approach, having larger convergence angles in mind, to horizontally displace the detector positions from the Thales circle position [2] in a direction closer to Bragg spots $\pm\mathbf{G}$ [12] and also move them slightly away from the systematic row. This is motivated by the expectation of a large nonmagnetic signal contribution originating from the disks at positions of the transmitted beam and Bragg spots, which will reduce the relative strength of the EMCD, particularly for larger convergence angles. This was qualitatively confirmed by a brief inspection of the 315 calculated energy-filtered diffraction patterns. The panels in Fig. 1(c) then show results for the marked detector apertures, where EMCD is obtained by a double-difference procedure [12]: if we denote the four quadrants of the diffraction pattern as *pp,mp,mm,mp* [see Fig. 2(a)], then the magnetic signal is extracted as $(pp + mm) - (pm + mp)$.

Results of the simulations show how the nonmagnetic signal grows with larger convergence angle, confirming that more and more of the intensity reaches the relatively displaced detector apertures. Importantly, it shows that a sizable magnetic signal can be expected for convergence semiangles well above 10 mrad, especially if the sample thickness stays below 30 nm. In relative terms the EMCD signal seems to be strongest for thicknesses around 10–20 nm and convergence semiangles up to 8 mrad. With increasing thickness and convergence angle the relative strength of EMCD decreases, but stays about $>2\%$ strong, except for the largest considered convergence angles and sample thicknesses. We note that for bcc iron in a systematic row orientation with $\mathbf{G} = (200)$, for convergence semiangles above 6.8 mrad the diffracted disks are overlapping, which means that in principle it is possible to detect signals with spatial resolution better than the lattice spacing.

III. EXPERIMENTS AND ANALYSIS

To verify the simulations, we have employed the STEM-EMCD technique. We utilized an FEI Tecnai F30 microscope operating at 300-kV acceleration voltage and equipped with a Gatan Tridiem spectrometer. This instrument does not have a probe aberration corrector, effectively limiting the convergence semiangles to below 12 mrad due to a spherical aberration of 1.2 mm. As a test sample, we used crystal of bcc iron with approximate thickness of 50 nm. Note that this thickness is greater than what is commonly used in EMCD experiments. The sample is an epitaxially grown thin film of iron on a MgO substrate, which was prepared in cross section for TEM measurements by dimple grinding and ion polishing using a Gatan PIPS. For a detailed description of the sample, we refer the reader to our recent work [18].

The experimental scattering conditions for the EMCD experiment are presented in Fig. 2(a). The sample was tilted to a three-beam geometry with the systematic row $\mathbf{G} = (200)$. The collection semiangle was set to 7.5 mrad by using

the spectrometer entrance aperture and changing the camera length. The convergence semiangle was set to 8.0 mrad by changing the current ratio between the objective and condenser lenses. A script was used to shift the diffraction pattern to the positions denoted by the red circles in Fig. 2(a), and four independent datacubes were acquired by utilizing the Gatan DIGISCAN software. The same survey image was used for all four datacubes, allowing for the same sample region to be rescanned. The step size for each pixel was set to 2 Å, each spectrum image consisted of 100 × 250 pixels, and the energy range covered by the spectra was 480–850 eV. The pixel dwell time was 0.02 s, and approximately 40 spectra per second were acquired with encoded spatial coordinates.

The high-angle annular dark field (HAADF) signal for each datacube is presented in Fig. 2(b), ordered in chronologically descending scan order from top to bottom. Immediately clear is the strong spatial drift between rows. An attempt was made to correct for these errors as best as possible during the data analysis, and this is presented in Fig. 2(c). The gradient of each row was computed in MATLAB and a cross correlation was performed over the Fe/MgO interface region to align the rows. While Fig. 2(c) reveals that the results of this analysis are reasonable, there are still clearly remaining errors, complicating a pixel-by-pixel analysis. This reduces the practical spatial resolution of this method to the area of summation, where spatial registration errors will be less influential. However, we also note that if the spatial drift could be reduced, the practical spatial resolution could be improved to the order of the pixel dimensions. An additional observation from Figs. 2(b) and 2(c) is that the contrast in the HAADF image appears to change as a function of number of scans. We interpret this as evidence for a modification of the TEM lamella due to the high electron dose. The influence of this beam damage on the quantification of m_L/m_S is unclear, but it degrades our confidence that the value we calculate here is free of artifacts.

Figure 2(d) demonstrates that a clear EMCD signal is extracted using a double-difference procedure [12]. Here, we again refer to the four quadrants as *pp*, *mm*, *pm*, *mp*, where *p* stands for "plus" and *m* for "minus". The spectra in Fig. 2(d) were generated by first adding the *pp* and *mm* datacubes, denoted as "even" here, and the *mp* and *pm* datacubes, denoted as "odd". Subsequently, all of the individual spectra in the "even" and "odd" datacubes were summed to generate a single spectrum from each. The pre-edge background was removed by extrapolating an inverse power-law model generated in the region between 660 and 700 eV underneath the iron ionization edges [23]. The background-subtracted spectra were then normalized to the postedge region of 750–800 eV and the difference was taken. This difference signal is known as the EMCD signal and its strength was determined by comparing the area under the Fe L_3 edge of the "even" spectrum to the area underneath the L_3 peak on the EMCD signal. We find that the EMCD signal strength is 3.6%, close to the value predicted by simulations [Fig. 1(c)]. Of note is that, despite the problems of beam damage noted above, a very reasonable value for m_L/m_S of 0.101 ± 0.014 is obtained by applying the EMCD sum rules [3,4]. The value is similar to what was previously obtained for bcc iron using EMCD [3,12,17]. Overestimation of the XMCD values can be explained by higher sample thickness and plural scattering effects [24].

The EMCD spectrum presented in Fig. 2 proves the primary finding of this paper, i.e., that it is possible for a nonzero EMCD signal to be generated in the classical three-beam geometry when utilizing electron-optical conditions that are sufficient for the resolution of individual atomic columns. Critically, this means that the ultimate fundamental spatial resolution of the EMCD technique must be better than the best experimentally reported values to date, which hover around the 1–2-nm scale [6,16]. However, at approximately 800 nm^2 (a circle with the same area has a diameter of 32 nm), the lateral area from which the spectra in Fig. 2(d) have been accumulated is not dramatically improved over what is possible with XMCD experiments, and nowhere near previous EMCD experiments. Below, we exploit the large number of spectra in these datasets to address the question of the minimum number of chirally scattered primary electrons necessary to unambiguously detect an EMCD signal of this strength using our experimental setup. This value is directly proportional to the scanned lateral area in this experimental design and is directly transferable to other systems.

We first cropped the "even" and "odd" datacubes to dimensions of 100 × 160 pixels, removing the Fe/MgO interface and the iron near the vacuum, leaving only the regions that can be considered "bulk" iron. We then started from the middle pixel and began summing different lateral areas ranging from 1 nm^2 to the full area of 640 nm^2. For simplicity, the summations were taken vertically along the columns of the datacubes. Following summation, the spectra were treated as described above and the EMCD signal extracted. The intensity of the spectra were captured in units of analogue digital counts (ADC) and subsequently converted to the number of primary electrons (pe^-) by using a conversion factor of 2.944 ADC/pe^-, which was calibrated by Gatan, Inc. For a quantifiable detection criterion, we calculated the SNR of the EMCD signal independently on the Fe L_3 and L_2 edge. This was accomplished by fitting a combination of two Gaussian peaks to the EMCD signal using the following expression:

$$f(E) = A_3 e^{-(\frac{E-\mu_3}{\sigma_3})^2} + A_2 e^{-(\frac{E-\mu_2}{\sigma_2})^2}. \quad (1)$$

Here, E represents the independent variable of energy, μ the centroid of both peaks, σ is related to the peak broadening, and A is the maximum value of the peaks. Subscripts 3 and 2 refer to the Fe L_3 and Fe L_2 edge, respectively. μ was constrained to lie between 706–715 eV for L_3 and 720–725 for L_2, σ was constrained to lie between 1.5–2.5 eV for both peaks, and A_3 was constrained to take on the opposite sign from A_2. The signal was defined as the value of parameters A for both peaks individually. An estimate of the noise was obtained by computing the standard deviation of the fit residuals in the range 660–730 eV. SNR is then defined as the ratio between the signal and this noise estimation. The total number of primary electrons contributing to the EMCD signal for both L_3 and L_2 was calculated by integrating the individual fitting curves. These electrons will be referred to as chirally scattered primary electrons.

In Fig. 3(a) we present a series of EMCD signals extracted after summing over different lateral areas. For each of these

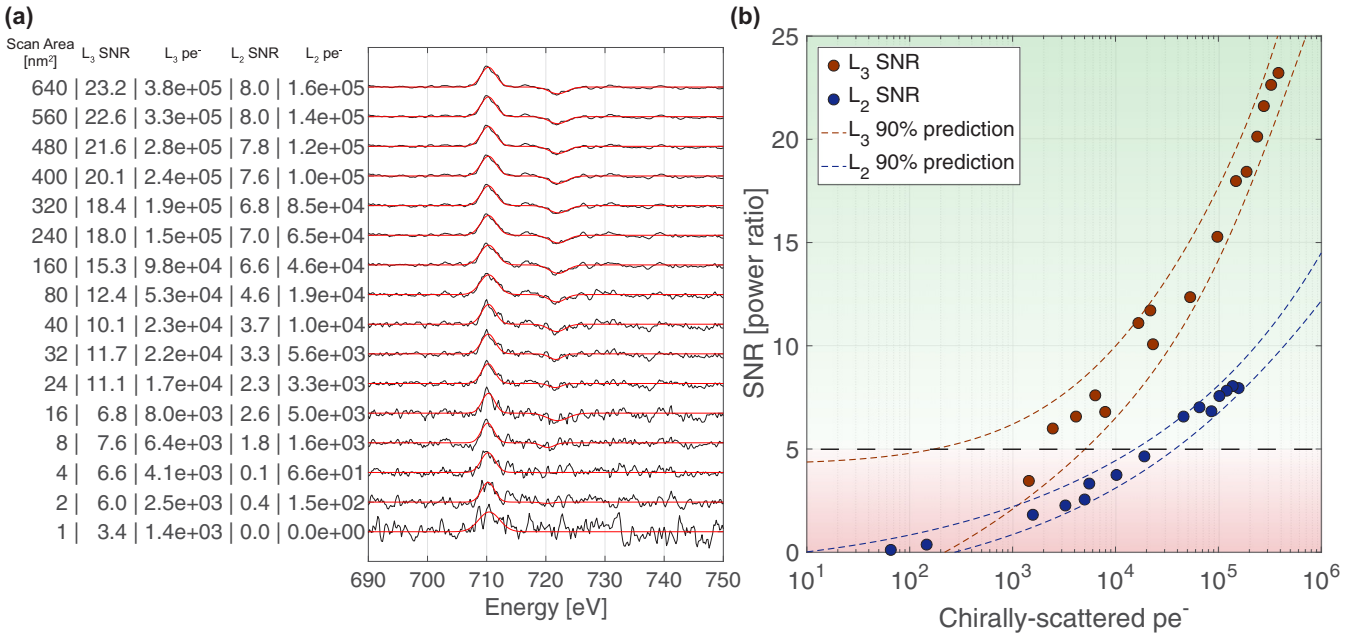

FIG. 3. (a) Examples of EMCD signals with the fitting curves from Eq. (1) overlaid in red color. The lateral scanning area for each curve is presented along with the SNR and number of chirally scattered primary electrons extracted from the fits independently for L_3 and L_2. (b) SNR for the EMCD signal on L_3 and L_2 edges as a function of the number of chirally scattered primary electrons. The dashed bounds represent a 90% prediction interval of the fit from Eq. (2). The Rose criterion of 5σ is denoted as a dashed horizontal line [25].

signals, the lateral scanning area used to acquire it is provided along with the SNR and the number of chirally scattered primary electrons under the L_3 and L_2 edges. The signal acquired from a summation of over 80 nm^2 clearly resolves an EMCD spectrum at both L_3 and L_2 edges. The data from the 1-nm^2 area still present an EMCD signal on the L_3 edge with an SNR of 3.4σ; however, nothing is visible on the L_2 edge and substantial noise levels are present. However, we note that this is superior to the previously reported spatial resolution record of 1.7 nm, which was determined only by taking a line scan across a thin layer of iron and showed similar noise characteristics [6].

The results of SNR analysis are summarized in Fig. 3(b). It is immediately evident that the EMCD signal is much easier to observe on the L_3 than the L_2 edge. This is because the absolute value of A_2 is smaller than A_3 due to the nonzero orbital moment, plural scattering effects [24], and spreading over a broader energy range due to a difference of core-hole lifetimes of the excitations from $2p_{1/2}$ levels compared to $2p_{3/2}$ ones. SNRs for both peaks roughly follow a power-law distribution,

$$\mathrm{SNR} = cN^r, \tag{2}$$

where c is a proportionality constant, r is the growth rate, and N represents the lateral sampling area. $r_{L_3} = 0.273 \pm 0.060$ and $r_{L_2} = 0.211 \pm 0.018$. The experimental values for both L_3 and L_2 are plotted in Fig. 3(b) along with a confidence interval of 90%. Note that both r_{L_3} and r_{L_2} are lower than the $\frac{1}{2}$ expected for purely statistical Poisson noise.

To define a detection threshold, we apply the the Rose criterion of 5σ, corresponding to a confidence level of 99.9999% [25]. Figure 3(b) reveals that we have a 90% chance of achieving this detection threshold on L_3 for summations over 8 nm^2, resulting in the collection of 6.4×10^3 electrons. This probability drops to approximately 50% for summations over 1 nm^2 area, where 1.4×10^3 electrons were detected. Hence, we can state that for an unambiguous detection of L_3, one needs to collect approximately 6400 chirally scattered electrons and that there is a reasonable chance of detection for less than 1500. However, it can be argued that to prove the existence of an EMCD signal, the SNR on *both* L_3 *and* L_2 must be higher than 5σ. To understand this, we can look to the SNR of the limiting L_2 edge, finding that we have a 50% chance of meeting the Rose criterion by summing over 100 nm^2, corresponding to a collection of approximately 2×10^4 chirally scattered primary electrons on this edge. Increasing the scanning area to 160 nm^2 brings this to a 90% chance.

IV. DISCUSSION AND OUTLOOK

Our experiments clearly show that an EMCD signal is generated when using electron-optical conditions sufficient for the resolution of atomic columns. This is demonstrated by using a convergence semiangle of 8 mrad, which at 300-kV acceleration voltage results in a probe of approximate FWHM of 2 Å if finite source broadening effects are neglected. The close match of this result with the simulations gives hope that even larger convergence angles can be used and that aberration-corrected TEMs can be employed in the near future to improve the beam coherency.

While the generation of this signal appears to be possible under these conditions, its detection is more challenging. The STEM-EMCD method we employ greatly assists with this, having the advantage of mitigating beam damage but requiring summation over large lateral areas to collect the large number

of chirally scattered electrons needed to improve the SNR. However, this allows us to explore the evolution of an EMCD signal from such datasets. Accordingly, we have presented a highly flexible detection scheme that can be used to quantify detection confidence from such datasets. Depending on how one defines a detection of an EMCD signal, one can claim that lateral areas as small as 1 nm^2 are sufficient with this method, with greatly improved confidence as larger areas are summed.

For experimental work, the SNR analysis presented in Fig. 3 can be used to estimate the total number of chirally scattered primary electrons needed to achieve a desired SNR. Dividing this number by the estimated EMCD signal strength (3.6% in our case), one can calculate the total number of primary electrons that would be present under the L_3 edge following background subtraction. This can then be directly related to the observed SNR for a raw spectrum on the microscope to provide an estimate for either total acquisition time or number of independent scans needed, acting as a strong assistant to the design of EMCD experiments.

While it may seem discouraging to accept that large lateral areas need to be summed to provide the SNR needed to achieve the Rose criterion, we note that these results are specific to a number of parameters in this particular experiment. If the EMCD signal strength were to increase above 3.6%, or if it becomes possible to improve the SNR for each individual spectra, for example, through the use of more efficient electron detectors, then the lateral scanning area needed to meet the Rose criterion would decrease accordingly. It is moreover noteworthy that, at 50 nm thick, this sample is among the thickest samples from which an EMCD analysis had been reported. Since the EMCD strength in general decreases for larger thicknesses, see Fig. 1(c) and Ref. [26], it is reasonable to expect that measurements on thinner samples would lead to a higher SNR due to the stronger EMCD signal, further improving the lateral scanning area needed for unambiguous detection. We interpret the detection of an EMCD signal with such a large sample thickness to underscore the efficiency of the STEM-EMCD method.

We also note that acquisition of such STEM EELS datasets gives the experimentalist a full flexibility in selecting an arbitrary lateral shape of the region of interest. For instance, one can select narrow rectangular areas in a scan across an interface or look for modifications of magnetism nearby localized features, such as vacancies or dislocations, or select data from an individual nanoparticle or grain.

Since the probe size achievable by this technique allows scanning with atomic resolution, it would be interesting to see such experiments performed on a state-of-the-art aberration-corrected microscope. Because these experiments are performed for samples tilted into systematic row orientation, the view of atomic columns is lost; however, in a symmetric three-beam geometry, the atomic planes would be resolvable. From a theoretical perspective, once the probe size approaches 1 Å and atomic planes become visible in the EEL spectrum images, an interesting question arises about the delocalization of the inelastic scattering signal, particularly for thicker samples [27].

V. CONCLUSIONS

In conclusion, we have presented theoretical simulations demonstrating that a non-negligible EMCD signal strength persists in bcc iron for a much larger range of convergence angles and thicknesses than previously thought. We confirmed this experimentally with an experiment carried out in the three-beam scattering geometry using the STEM-EMCD setup, demonstrating an EMCD signal strength in agreement with theoretical predictions. Subsequent analysis of the EMCD datacube reveals that it is possible to quantify the confidence of EMCD signal detection. We demonstrate that for an EMCD signal strength of 3.6%, several tens of thousands of chirally scattered electrons should guarantee a clear EMCD signal on L_2, while about 6500 should be sufficient to detect EMCD on L_3. This paves the road for classical EMCD experiments using a subnanometer electron probe and exceptionally high spatial resolution.

ACKNOWLEDGMENTS

The authors thank the Swedish Research Council, Göran Gustafsson's Foundation, and the Swedish Foundation for International Cooperation in Research and Higher Education IG2009-2017 for financial support. The authors acknowledge Sharath Kumar for preparation of the TEM lamella. The simulations were performed on resources provided by the Swedish National Infrastructure for Computing (SNIC) at the National Supercomputer Centre (NSC) at Linköping University.

[1] P. Gambardella, A. Dallmeyer, K. Maiti, M. C. Malagoli, W. Eberhardt, K. Kern, and C. Carbone, Nature (London) **416**, 301 (2002).

[2] P. Schattschneider, S. Rubino, C. Hébert, J. Rusz, J. Kuneš, P. Novák, E. Carlino, M. Fabrizioli, G. Panaccione, and G. Rossi, Nature (London) **441**, 486 (2006).

[3] L. Calmels, F. Houdellier, B. Warot-Fonrose, C. Gatel, M. J. Hÿtch, V. Serin, E. Snoeck, and P. Schattschneider, Phys. Rev. B **76**, 060409(R) (2007).

[4] J. Rusz, O. Eriksson, P. Novák, and P. M. Oppeneer, Phys. Rev. B **76**, 060408(R) (2007).

[5] C. Hébert and P. Schattschneider, Ultramicroscopy **96**, 463 (2003).

[6] P. Schattschneider, M. Stöger-Pollach, S. Rubino, M. Sperl, C. Hurm, J. Zweck, and J. Rusz, Phys. Rev. B **78**, 104413 (2008).

[7] P. Schattschneider, C. Hébert, S. Rubino, M. Stöger-Pollach, J. Rusz, and P. Novák, Ultramicroscopy **108**, 433 (2008).

[8] Z. Q. Wang, X. Y. Zhong, R. Yu, Z. Y. Cheng, and J. Zhu, Nat. Commun. **4**, 1395 (2013).

[9] K. Tatsumi, S. Muto, J. Rusz, T. Kudo, and S. Arai, Microscopy (Tokyo) **63**, 243 (2014).

[10] W. Chao, P. Fischer, T. Tyliszczak, S. Rekawa, E. Anderson, and P. Naulleau, Opt. Express **20**, 9777 (2012).

[11] P. Fischer, Front. Phys. **2**, 82 (2015).

[12] H. Lidbaum, J. Rusz, A. Liebig, B. Hjörvarsson, P. M. Oppeneer, E. Coronel, O. Eriksson, and K. Leifer, Phys. Rev. Lett. **102**, 037201 (2009).

[13] B. Loukya, X. Zhang, A. Gupta, and R. Datta, J. Magn. Magn. Mater. **324**, 3754 (2012).

[14] H. Lidbaum, J. Rusz, S. Rubino, A. Liebig, B. Hjörvarsson, P. M. Oppeneer, O. Eriksson, and K. Leifer, Ultramicroscopy **110**, 1380 (2010).
[15] M. Stöger-Pollach, C. Treiber, G. Resch, D. Keays, and I. Ennen, Micron **42**, 456 (2011).
[16] J. Salafranca, J. Gazquez, N. Pérez, A. Labarta, S. T. Pantelides, S. J. Pennycook, X. Batlle, and M. Varela, Nano Lett. **12**, 2499 (2012).
[17] S. Muto, J. Rusz, K. Tatsumi, R. Adam, S. Arai, V. Kocevski, P. M. Oppeneer, D. E. Bürgler, and C. M. Schneider, Nat. Commun. **5**, 3138 (2014).
[18] T. Thersleff, J. Rusz, S. Rubino, B. Hjörvarsson, Y. Ito, N. J. Zaluzec, and K. Leifer, Sci. Rep. **5**, 13012 (2015).
[19] O. Krivanek, G. Corbin, N. Dellby, B. Elston, R. Keyse, M. Murfitt, C. Own, Z. Szilagyi, and J. Woodruff, Ultramicroscopy **108**, 179 (2008).
[20] M. Haider, P. Hartel, H. Müller, S. Uhlemann, and J. Zach, Microsc. Microanal. **16**, 393 (2010).
[21] J. Rusz, S. Bhowmick, M. Eriksson, and N. Karlsson, Phys. Rev. B **89**, 134428 (2014).
[22] J. Verbeeck, C. Hébert, S. Rubino, P. Novák, J. Rusz, F. Houdellier, C. Gatel, and P. Schattschneider, Ultramicroscopy **108**, 865 (2008).
[23] R. F. Egerton, *Electron Energy-Loss Spectroscopy in the Electron Microscope* (Springer, New York, 2011).
[24] J. Rusz, H. Lidbaum, S. Rubino, B. Hjörvarsson, P. M. Oppeneer, O. Eriksson, and K. Leifer, Phys. Rev. B **83**, 132402 (2011).
[25] A. Rose, *Vision: Human and Electronic, Optical Physics and Engineering* (Plenum Press, New York, 1973).
[26] J. Rusz, S. Rubino, and P. Schattschneider, Phys. Rev. B **75**, 214425 (2007).
[27] L. J. Allen, S. D. Findlay, A. R. Lupini, M. P. Oxley, and S. J. Pennycook, Phys. Rev. Lett. **91**, 105503 (2003).